Journal of Quantitative Spectroscopy & Radiative Transfer 117 (2013) 59–70

Contents lists available at SciVerse ScienceDirect

Journal of Quantitative Spectroscopy & Radiative Transfer

journal homepage: www.elsevier.com/locate/jqsrt

A hybrid method for modeling polarized radiative transfer in a spherical-shell planetary atmosphere

Feng Xu [a,b,*], Robert A. West [a], Anthony B. Davis [a]

[a] Jet Propulsion Laboratory, California Institute of Technology, Pasadena, CA 91109, USA
[b] Joint Institute for Regional Earth System Science and Engineering, University of California, Los Angeles, CA 90095, USA

ARTICLE INFO

Article history:
Received 2 August 2012
Received in revised form
16 October 2012
Accepted 17 October 2012
Available online 20 November 2012

Keywords:
Polarized radiative transfer
Spherical-shell atmosphere
Picard iteration
Pseudo-spherical approximation
Titan haze

ABSTRACT

The Markov chain method is developed for polarized radiative transfer in a pseudo-spherical atmosphere with solar illumination. This solution is then used as an initial guess of the radiation field for a spherical atmosphere. By use of the short characteristic method, a convergent radiation field throughout the atmosphere is achieved after a few Picard iterations. We verified this hybrid method by comparing numerical results to those obtained by a backward Monte Carlo calculation. We carried out a demonstration calculation by simulating the Titan haze reflected intensity I and Stokes parameter Q, and degree of linear polarization at 934.8 nm wavelength. Comparison of the I and Q images to those measured by the Imaging Science Subsystem instrument on the Cassini spacecraft shows the hybrid method to be useful for radiative transfer analyses for (both optically and physically) thick spherical atmospheres.

1. Introduction

Retrievals of planetary atmosphere and surface properties from photometric and polarimetric data requires a reliable radiative transfer (RT) model for radiance and polarization computation. To ensure accuracy of the forward computation of the limb radiance and to constrain the solution including linear polarization, a polarized radiative transfer model that accounts for atmospheric sphericity and radial inhomogeneity is required. Compared to the variety of numerical methods available for plane-parallel geometry, numerical solutions for the spherical atmosphere are very limited due to the more complex 2-dimensional (2D) nature of the spatial RT problem.

By partially accounting for the spherical geometry, some approximate methods have been studied for the 2D RT. For example, a pseudo-spherical solution was developed [1] by accounting for the incident solar beam attenuation and single scattering in full spherical geometry and then retaining the assumption of a segmented plane-parallel structure for multiple scattering. For ozone retrieval using ultraviolet radiance, such a solution was reported [2,3] to have small errors as the viewing angle gets close to nadir viewing angles at high Sun condition. However, considerable error occurs at limb viewing angles for low solar illumination, which leads to large uncertainties in the aerosol retrieved from limb radiance. For some planets of large atmosphere-thickness-to-planet-radius ratio (which can be 500/2576 for Titan), the limb or terminator radiance errors of the pseudo-spherical approximation are even more obvious than that for Earth ($\approx$ 100/6371). Indeed, the increased curvature of planet and atmosphere impedes the application of pseudo-spherical solutions [2–4] to Titan's atmosphere in their present form. However, the pseudo-spherical solutions can be used to initialize the accurate iterative solutions to RT in a spherical atmosphere.

To account for the atmospheric sphericity in an exact way, the forward or backward Monte Carlo method has

* Corresponding author at: Jet Propulsion Laboratory, California Institute of Technology, Pasadena, CA 91109, USA.
E-mail address: Feng.Xu@jpl.nasa.gov (F. Xu).

0022-4073/$ - see front matter © 2012 Elsevier Ltd. All rights reserved.
http://dx.doi.org/10.1016/j.jqsrt.2012.10.013

been applied to Earth and planetary atmospheres [5–7]. In terms of computational efficiency, however, the deterministic methods, e.g. successive orders of scattering [8], Gauss–Seidel iteration [9,10], and Picard iteration (or Lambda iteration) [11,12] have advantages. Of high relevancy to our work is the Picard iteration scheme based on the long characteristic method (LCM) or the short characteristic method (SCM). In the LCM [13], the intersection point of a characteristic line with the atmosphere boundary is taken as the reference point and the radiation field at a current grid point is obtained by calculating recursively the radiation field at the intersection points of the characteristic line with all spherical interfaces. Such a method was adopted to study the radiative transfer in Titan's atmosphere overlying a Lambertian surface [14]. To improve the convergence the SCM was proposed [15], which differs from the LCM in that during the inward/outward recurrence the intersections of the characteristic lines with outer/inner interfaces of a sub-layer are taken as the reference points. This way the multiple scattering component of the radiation field at the reference point is updated during the recurrence. Starting with a proper initial guess of the radiation field throughout the atmosphere, the convergent solution is expected to be obtained in a few iterations.

This paper aims to extend the SCM-based Picard iteration for polarized radiative transfer in a spherical-shell atmosphere overlying a polarizing or depolarizing planetary surface (the term "spherical-shell atmosphere" means that the atmospheric properties vary only along the radial direction and are modeled as a collection of homogeneous spherical shells). In Section 2 we give the Markov chain formalism for calculating the radiation field inside the plane-parallel atmosphere, and then give the correction to get the pseudo-spherical solution. Initialized by the pseudo-spherical solution the SCM-based Picard iteration scheme is described in Section 3 to get an accurate solution to the full-spherical atmosphere. In Section 4, our method is verified through comparing its numerical results to those obtained by the Monte Carlo method and then demonstrated by comparison of simulated and real intensity and polarization images of Titan's haze. A summary and outline of future work is given in Section 5.

2. Markov chain formulation of polarized radiative transfer

The Markov chain method was initially proposed to compute scalar radiative transfer in a plane-parallel atmosphere [16,17]. With the implementation of a "chain-to-chain adding strategy", its application in computing radiative transfer through Venus' atmosphere shows higher computation efficiency than that of adding/doubling method [17]. Though the total field is most generally obtained through a matrix inverse operation, the Markov Chain RT formalism can be cast in terms of the contributions of different orders of scattering [16]. Since the inverse matrix is independent of the solar incidence angle, the radiation field along different radial lines in a spherical atmosphere can be initialized immediately. Based on its characteristic basis in matrix algebra, the Markov Chain method lends itself readily to implementation on a graphics processing unit (GPU) for future high-speed computations. Moreover, it can be extended to three-dimensional radiative transfer problems because, like the Monte Carlo method, it deals directly with probabilities of transition between states in transport space (position, direction).

2.1. Plane-parallel atmosphere

Assume that a vertically inhomogeneous plane-parallel atmosphere of optical depth τ_0 is divided into $N-1$ atmospheric sub-layers so that each one has the optical thickness $\Delta\tau_n=\tau_{n+1}-\tau_n\,(1\le n\le N-1)$ and $\tau_N=\tau_0$. Further assuming the Nth layer to be the reflecting surface, it has no thickness so that $\Delta\tau_N=0$. The light direction is described by the zenith and azimuth angles v,ϕ respectively. Following Chandrasekhar's convention [18], the incident solar flux is πF. The light propagation direction within the atmosphere is discretized into N_μ angles over the range $0\le\mu\le1$, where $\mu=|u|=|\cos v|$, and v is the angle of propagation relative to the downward normal. After a Fourier series expansion in the difference between the view and incident azimuthal angles, $\phi-\phi_0$, the "state" of the radiant energy deposited in each Fourier mode is described by its location layer (indexed by n) and its direction of propagation u_i. In the Markov chain method, the transition probability from one state (n, u_i) to another (n', u_j) is given by the transition matrix $\mathbf{Q}$ and the distribution of initial states (from single scattering) is denoted by $\mathbf{\Pi}_0$. To specify the dimension of the matrix used in the Markov chain formalism, we define $N_D=N\cdot N_m\cdot N_d\cdot N_\mu\cdot N_{Stokes}$ where N_m is the number of Fourier series modes which can be cosine (denoted by subscript "c") or sine ("s") so that $N_m=2$, N_d is the light propagation direction which can be upwelling or downwelling so that $N_d=2$, and the dimension number for Stokes vector represented by the column vector $[I, Q, U, V]^T$ is $N_{Stokes}=4$. Defining the Stokes vector with respect to the meridian plane, the radiation field inside the atmosphere (or "internal field") is then expressed independently for each azimuthal component m as a consequence of matrix operations on the matrix $\mathbf{\Pi}_0^{(m)}$ of dimension $N_D\times N_\mu$ and the matrix $\mathbf{Q}^{(m)}$ of dimension $N_D\times N_D$ [19,20]:

$$\mathbf{I}_{in}^{(m)}=\left(\mathbf{E}-\mathbf{Q}^{(m)}\right)^{-1}\mathbf{\Pi}_0^{(m)} \tag{1}$$

where $\mathbf{E}$ is the identity matrix of dimension $N_D\times N_D$, and the solution vector $\mathbf{I}_{in}^{(m)}$ of dimension $N_D\times1$ is formed by the cosine mode ($\mathbf{I}_{in,c}^{(m)}$) and sine mode ($\mathbf{I}_{in,s}^{(m)}$) of the Fourier component of the radiation field emergent from an atmospheric layer due to the extinction and scattering processes in it. With $\mathbf{I}_{in,c/s}^{(m)}$ determined from Eq. (1), the diffuse radiation field emergent from nth layer in direction u_j is

$$\begin{aligned}\mathbf{I}_{in}(\Delta\tau_n,u_j,u_0,\phi-\phi_0)&=\sum_{m=0}^{\infty}\frac{(2-\delta_{0m})}{2w_j\mu_j}\Big[\mathbf{I}_{in,c}^{(m)}(\Delta\tau_n,u_j,u_0)\cos m(\phi-\phi_0)\\&+\mathbf{I}_{in,s}^{(m)}(\Delta\tau_n,u_j,u_0)\sin m(\phi-\phi_0)\Big],\end{aligned} \tag{2}$$

where δ_{0m} is the Kronecker delta symbol and w_j is the quadrature weight at μ_j. Calculation of all matrices was given previously [19,20]. Note that the radiation field obtained from Eqs. (1) and (2) is at the N_μ discretized angles. To accurately evaluate the radiation field at arbitrary viewing and incidence angles, Eq. (1) has to be generalized to be

$$\mathbf{I}_{\text{in}}^{(m)} = \mathbf{Q}_{\text{v}}^{(m)} \left(\mathbf{E} - \mathbf{Q}^{(m)}\right)^{-1} \mathbf{\Pi}_{0}^{(m),i} + \mathbf{\Pi}_{0,\text{v}}^{(m),i} \tag{3}$$

where the matrices $\mathbf{Q}_{\text{v}}^{(m)}$, $\mathbf{\Pi}_{0}^{(m),i}$, and $\mathbf{\Pi}_{0,\text{v}}^{(m),i}$ have the dimensions $N_{\text{v}} \times N_{\text{D}}$, $N_{\text{D}} \times N_{\text{inc}}$ and $N_{\text{v}} \times N_{\text{inc}}$ respectively, with N_{inc} being the number of incidence angles and $N_{\text{v}} = N \cdot N_m \cdot N_{\text{d}} \cdot N_{\text{view}} \cdot N_{\text{Stokes}}$, with N_{view} being the number of viewing angles. Their computation differs from the computation of $\mathbf{Q}^{(m)}$ and $\mathbf{\Pi}_{0}^{(m)}$ by using the cosines of the given viewing and/or incidence angles.

The total radiation field emergent from the boundaries of the nth layer is a sum over the contribution from all upper or lower layers, namely

$$\mathbf{I}_{\text{in}}^{-}\left(\tau_{n+1}, \mu_j, \mu_0, \phi - \phi_0\right) = \sum_{k=1}^{n} \mathbf{I}_{\text{in}}\left(\Delta\tau_k, \mu_j, \mu_0, \phi - \phi_0\right) \times c\left(\Delta\tau_k, \mu_j\right) \exp[-(\tau_n - \tau_k)/\mu_j], \tag{4}$$

for downwelling ("−") light, and

$$\mathbf{I}_{\text{in}}^{+}\left(\tau_n, \mu_j, \mu_0, \phi - \phi_0\right) = \sum_{k=n}^{N} \mathbf{I}_{\text{in}}\left(\Delta\tau_k, -\mu_j, \mu_0, \phi - \phi_0\right) \times c\left(\Delta\tau_k, \mu_j\right) \exp[-(\tau_k - \tau_n)/\mu_j] \tag{5}$$

for upwelling ("+") light. Note that Eqs. (1) and (3) are based on a constant source function assumption throughout a sub-layer, and the correction factor $c(\Delta\tau_k, \mu_j)$ in Eqs. (4) and (5) is introduced to get the radiance emergent from the layer boundaries:

$$c\left(\Delta\tau_k, \mu_j\right) = \begin{cases} \frac{\mu_j}{\Delta\tau_k}\left[1 - \exp\left(-\frac{\Delta\tau_k}{\mu_j}\right)\right], & k \le N-1 \\ 1, & k = N. \end{cases} \tag{6}$$

As an important characteristic of the Markov chain method, the matrix inverse $(\mathbf{E} - \mathbf{Q}^{(m)})^{-1}$ is invariant to incident light profiles. This means that, once the matrix inverse is determined, the radiation field for different incidence angles (or more specifically, for different initial distributions of light in the atmosphere, Π_0's) can be obtained in an efficient way. This greatly improves the speed of computing the radiation field along different radial lines in a pseudo-spherical atmosphere since only solar incidence angle changes for different sets of plane-parallel atmosphere systems set up along the radial lines.

2.2. Pseudo-spherical atmosphere

In a spherical atmosphere, the radial, angular and azimuthal coordinates R, Θ and Φ are used as global coordinates to specify a point with the position vector $\boldsymbol{R}$ with $\boldsymbol{R}/R = (\sin\Theta\cos\Phi, \sin\Theta\sin\Phi, \cos\Theta)$. Dividing the atmosphere into N–1 layers, setting the Nth layer to be the planetary surface, and discretizing Θ into N_Θ radial lines in the domain $0 \le \Theta \le 180^\circ$ and Φ into N_Φ azimuthal planes in the domain $0 \le \Phi \le 360^\circ$, the atmosphere has $N \cdot N_\Theta \cdot N_\Phi$ grid points, each one specified by (R_n, Θ_j, Φ_k) where $1 \le n \le N$, $1 \le j \le N_\Theta$ and $1 \le k \le N_\Phi$. In the spherical shell approximation the atmospheric properties are considered to be a function only of the layer number n. Then the single scattering albedo (SSA) $\omega_0(\boldsymbol{R}) \equiv \omega_0(n)$, the extinction coefficient $\sigma(\boldsymbol{R}) \equiv \sigma(n)$, and the phase matrix $\mathbf{M}(\mathbf{\Omega}_{\text{G}}, \mathbf{\Omega}_{\text{G},0}; \boldsymbol{R}) \equiv \mathbf{M}(\mathbf{\Omega}_{\text{G}}, \mathbf{\Omega}_{\text{G},0}; n)$, where $\mathbf{\Omega}_{\text{G},0}$ denotes the Sun direction in global spherical coordinate system (R, Θ, Φ). Setting the OZ axis of the global coordinate system oriented toward the Sun (see Fig. 1), we have $\mathbf{\Omega}_{\text{G},0} = [0, 0, -1]^{\text{T}}$ and the radiation field for solar illumination has cylindrical symmetry so that the Φ coordinate in the global coordinate system is not needed.

To specify the direction of diffuse light in local spherical coordinate system set up at each grid point, the angular coordinates θ and ϕ are used as the local viewing and azimuthal angles (see Fig. 1) so that the direction in local coordinate system is $\mathbf{\Omega}_{\text{L}} = (\sin\theta\cos\phi, \sin\theta\sin\phi, \cos\theta)^{\text{T}}$ and $\phi = 0$ and π denote the local principal plane containing the direction of the solar beam and the surface normal at the grid point.

At any grid point A, $\mathbf{\Omega}_{\text{L}}$ can be converted to its counterpart $\mathbf{\Omega}_{\text{G}}$ in global coordinate system via a rotation matrix $\mathbf{B}$, namely, $\mathbf{\Omega}_{\text{G}} = \mathbf{B} \cdot \mathbf{\Omega}_{\text{L}}$, where as a function of $\boldsymbol{R}_{\text{A}}$, $\mathbf{B}$ is expressed as [22]

$$\mathbf{B}(\boldsymbol{R}_{\text{A}}) = \begin{bmatrix} \cos\Theta_{\text{A}}\cos\Phi_{\text{A}} & -\sin\Phi_{\text{A}} & \sin\Theta_{\text{A}}\cos\Phi_{\text{A}} \\ \cos\Theta_{\text{A}}\sin\Phi_{\text{A}} & \cos\Phi_{\text{A}} & \sin\Theta_{\text{A}}\sin\Phi_{\text{A}} \\ -\sin\Theta_{\text{A}} & 0 & \cos\Theta_{\text{A}} \end{bmatrix} \tag{7}$$

and vice versa, $\mathbf{\Omega}_{\text{L}} = \mathbf{B}^{-1} \cdot \mathbf{\Omega}_{\text{G}}$.

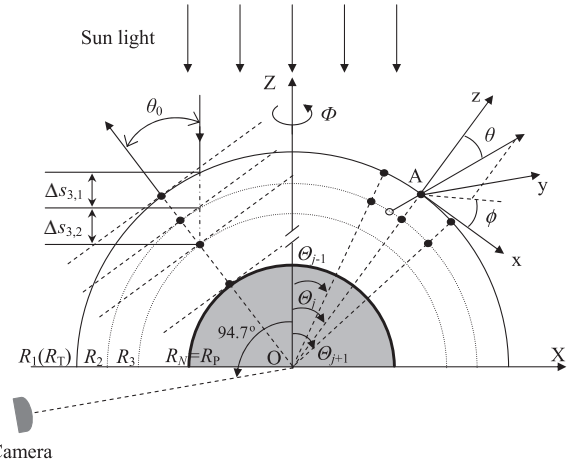

Fig. 1. Global (XYZ) and local (xyz) coordinate systems set up for computing the radiation field in a spherical atmosphere and in a pseudo-spherical atmosphere. The spherical atmosphere in divided into $N-1$ layers with the radii R_1 ($R_1 = R_{\text{T}}$), R_2, R_3, … and R_N ($R_N = R_{\text{P}}$) for spherical interfaces from the top to the bottom of the atmosphere. The OZ axis of the global coordinate system O-XYZ is oriented toward the Sun and (Θ, Φ) specify the global angular coordinates of a point. Some grid points (R_n, Θ_j, Φ_k) are denoted by black dots. At any grid point (e.g., point A in the schematic) a local coordinate system A-xyz is set up where (θ, ϕ) are local angular coordinates specifying the diffuse light direction. In the left half of the figure, a plane-parallel atmosphere is set up referring to the grid points along the same radial line to compute the multiple scattering field for the solution to the pseudo-spherical atmosphere. The Cassini camera images of Titan shown below were obtained at phase angle 94.7°.

To compute radiation field in a pseudo-spherical atmosphere, the multiple scattering field at the set of grid points along a radial line (say $\Theta=\Theta_j$) is approximated by the multiple scattering field in a plane-parallel atmosphere oriented perpendicular to the radial line at these grid points (see Fig. 1). Under this situation, the solar incidence angle $v_0=\Theta_j$. To improve the approximation, the state vector $\mathbf{\Pi}_0$ is modified by introducing the probability of solar beam transmission from the incident point s' at the top of atmosphere to a point s at the outer boundary of a layer inside the atmosphere, namely [2],

$$T(s)=\exp\left[-\int_{s'}^{s}\sigma(s')ds'\right] \tag{8}$$

where the extinction coefficient $\sigma=\kappa_T\rho$, with κ_T and ρ being the total mass extinction coefficient and the total mass density, respectively. For a given Fourier component, the initial state vector is computed by single scattering due to extinction in the nth layer, namely

$$\mathbf{\Pi}^{(m),+}_{0,c/s}(\Delta\tau_n,\mu_i,\mu_0)=\frac{w_i}{c(\Delta\tau_n,\mu_i)}\frac{\mu_0\mu_i}{\mu_i+\mu_0}T(s_n)\omega_0(n)\times\left\{1-\exp\left[-\Delta\tau_n\left(\frac{1}{\mu_0}+\frac{1}{\mu_i}\right)\right]\right\}\frac{\mathbf{M}^{(m)}_{c/s}(-\mu_i,\mu_0;n)}{2}\boldsymbol{F} \tag{9}$$

for outward radiation and

$$\mathbf{\Pi}^{(m),-}_{0,c/s}(\Delta\tau_n,\mu_i,\mu_0)=\frac{w_i}{c(\Delta\tau_n,\mu_i)}\frac{\mu_0\mu_i}{\mu_i-\mu_0}T(s_n)\omega_0(n)\times\left\{\exp\left(-\frac{\Delta\tau_n}{\mu_i}\right)-\exp\left(-\frac{\Delta\tau_n}{\mu_0}\right)\right\}\frac{\mathbf{M}^{(m)}_{c/s}(\mu_i,\mu_0;n)}{2}\boldsymbol{F} \tag{10a}$$

$$\mathbf{\Pi}^{(m),-}_{0,c/s}(\Delta\tau_n,\mu_i,\mu_0)=\frac{w_i}{c(\Delta\tau_n,\mu_i)}T(s_n)\omega_0(n)\times\left[\Delta\tau_n\exp\left(-\frac{\Delta\tau_n}{\mu_i}\right)\right]\frac{\mathbf{M}^{(m)}_{c/s}(\mu_i,\mu_0;n)}{2}\boldsymbol{F} \tag{10b}$$

for inward radiation, when $\mu_i\neq\mu_0$ and $\mu_i=\mu_0$, respectively, where $\omega_0(n)$ is the SSA of the nth atmospheric layer, $\mathbf{M}^{(m)}_{c/s}(\mu_i,\mu_0;n)$ is the cosine ("c") or sine ("s") mode of the mth Fourier component of the phase matrix describing light scattering from direction μ_0 to μ_i, and $\boldsymbol{F}=[F,0,0,0]^T$. Decomposing the phase matrix for surface reflection $\mathbf{M}_{surf}$ into Fourier components $\mathbf{M}^{(m)}_{surf,c/s}$, the initial state of surface-reflected light is

$$\mathbf{\Pi}^{(m),+}_{0,c/s}(0,\mu_i,\mu_0)=2w_iT(s_N)\mathbf{M}^{(m)}_{surf,c/s}(-\mu_i,\mu_0)\mu_0\mu_i\boldsymbol{F} \tag{11}$$

The line integral in Eq. (8) can be broken into a set of segments in different sub-layers so that the total optical path can be approximated by summing over the optical depth in different sub-layers and for $n\geq 2$ [21]

$$T(s_n)\approx\exp\left(-\sum_{k=1}^{n-1}\sigma_k\Delta s_{n,k}\right), \tag{12}$$

where the length of line segment in kth sub-layer $\Delta s_{n,k}$ (see Fig. 1) can be determined via the following equation after invoking some basic triangular relations,

$$\Delta s_{n,k}=\left(R_k^2-R_n^2\sin^2v_0\right)^{1/2}-\left(R_{k+1}^2-R_n^2\sin^2v_0\right)^{1/2}. \tag{13}$$

For $n=1$, $T(s_n)=1$. When the planet radius R_P approaches infinity the spherical atmosphere tends to be plane-parallel and $T(s_n)$ can be evaluated analytically by $\exp(-\tau_n/\mu_0)$.

After the total radiation field for a plane-parallel atmosphere is obtained by using Eqs. (9)–(11) and Eqs. (1)–(5), the single scattering contribution needs to be replaced by the one evaluated in a full spherical atmosphere so that the inward radiation field in the pseudo-spherical atmosphere is

$$\mathbf{I}^-_{in}\left(\tau_{n+1},\mu_j,\mu_0,\phi-\phi_0\right)=\mathbf{I}_{ss,sph}(\boldsymbol{R}_{n+1},\boldsymbol{R}_T;\mathbf{\Omega}_G)+\sum_{k=1}^{n}[\mathbf{L}(\pi-\beta)]^{-1}[\mathbf{I}^-_{in}\left(\Delta\tau_k,\mu_j,\mu_0,\phi-\phi_0\right)-\mathbf{I}^-_{in,ss}\left(\Delta\tau_k,\mu_j,\mu_0,\phi-\phi_0\right)]c\left(\Delta\tau_k,\mu_j\right)\exp[-(\tau_n-\tau_k)/\mu_j] \tag{14}$$

and the outward radiation field is

$$\mathbf{I}^+_{in}\left(\tau_n,\mu_j,\mu_0,\phi-\phi_0\right)=\mathbf{I}_{ss,sph}(\boldsymbol{R}_n,\boldsymbol{R}_{T/B};\mathbf{\Omega}_G)+\sum_{k=n}^{N}[\mathbf{L}(\pi-\beta)]^{-1}[\mathbf{I}^+_{in}\left(\Delta\tau_k,\mu_j,\mu_0,\phi-\phi_0\right)-\mathbf{I}^+_{in,ss}\left(\Delta\tau_k,\mu_j,\mu_0,\phi-\phi_0\right)]c\left(\Delta\tau_k,\mu_j\right)\exp[-(\tau_k-\tau_n)/\mu_j], \tag{15}$$

where the following single-scattering field in the plane-parallel atmosphere

$$\mathbf{I}_{in,ss}(\Delta\tau_n,u_j,u_0,\phi-\phi_0)=\sum_{m=0}^{\infty}\frac{(2-\delta_{0m})}{2w_j\mu_j}\left[\mathbf{\Pi}^{(m)}_{0,c}(\Delta\tau_n,u_j,u_0)\cos m(\phi-\phi_0)+\mathbf{\Pi}^{(m)}_{0,s}(\Delta\tau_n,u_j,u_0)\sin m(\phi-\phi_0)\right] \tag{16}$$

is replaced by the one evaluated in the full spherical geometry, namely

$$\mathbf{I}_{ss,sph}(\boldsymbol{R},\boldsymbol{R}_{T/B};\mathbf{\Omega}_G)=\int_0^{\|\boldsymbol{R}-\boldsymbol{R}_{T/B}\|}\mathbf{J}_{ss,sph}(\boldsymbol{R}(\ell),\mathbf{\Omega}_G)\times\exp\left[-\int_{\|\boldsymbol{R}(\ell)-\boldsymbol{R}_{T/B}\|}^{\|\boldsymbol{R}-\boldsymbol{R}_{T/B}\|}\sigma(\boldsymbol{R}(\ell'))d\ell'\right]d\ell, \tag{17}$$

where $\boldsymbol{R}$ and $\mathbf{\Omega}_G$ denote the position and direction respectively where single scattering is calculated, $\boldsymbol{R}_{T/B}$ is the position vector of the point at the top ($\boldsymbol{R}_T$) or bottom ($\boldsymbol{R}_B$) of the atmosphere where the line integral starts and ($\boldsymbol{R}-\boldsymbol{R}_{T/B}$) is in the direction of solar beam $\mathbf{\Omega}_G$, namely $\boldsymbol{R}(\ell)=\boldsymbol{R}_{T/B}+\mathbf{\Omega}_G\ell$ and the single scattering source function, $\mathbf{J}_{ss,sph}$, for example, is evaluated by

$$\mathbf{J}_{ss,sph}(\boldsymbol{R},\mathbf{\Omega}_G)=\frac{1}{4}\exp\left[-\int_0^{\|\boldsymbol{R}-\boldsymbol{R}'_T\|}\sigma(\boldsymbol{R}'(\ell))d\ell\right]\times\sigma(\boldsymbol{R})\omega_0(\boldsymbol{R})\mathbf{M}(\mathbf{\Omega}_G,\mathbf{\Omega}_{G,0};\boldsymbol{R})\boldsymbol{F} \tag{18}$$

for $\boldsymbol{R}$ in the lit region of the atmosphere, where $\boldsymbol{R}'(\ell)=\boldsymbol{R}'_T+\mathbf{\Omega}_{G,0}\ell$ ($\boldsymbol{R}'_T$ is the position vector of the point at the top of the atmosphere that leads ($\boldsymbol{R}-\boldsymbol{R}'_T$) to be in the direction of solar beam $\mathbf{\Omega}_{G,0}$). Since the Stokes vector of the radiation field in the spherical atmosphere (including the single scattering calculated by Eq. (17)) is defined with respect to the plane containing the incident OZ axis and diffuse light direction while its counterpart in the plane-parallel atmosphere is defined with respect to the meridian plane in local coordinate system of the grid points, a rotation matrix $[\mathbf{L}(\pi-\beta)]^{-1}$ is used in Eqs. (14)–(15) for conversion. Specifically

$\mathbf{L}(\pi-\beta)=[1,\ 0,\ 0,\ 0;\ 0,\ \cos(2\beta),\ -\sin(2\beta),\ 0;\ 0,\ \sin(2\beta),\ \cos(2\beta),\ 0;\ 0,\ 0,\ 0,\ 1]$ with $\cos\beta=(\boldsymbol{\Omega}_{\mathrm{G}}\times\boldsymbol{R})\cdot(\boldsymbol{\Omega}_{\mathrm{G}}\times\boldsymbol{\Omega}_{\mathrm{G},0})/\|\boldsymbol{\Omega}_{\mathrm{G}}\times\boldsymbol{R}\|/\|\boldsymbol{\Omega}_{\mathrm{G}}\times\boldsymbol{\Omega}_{\mathrm{G},0}\|$.

3. Spherical atmosphere

The SCM-based Picard iteration for computing polarized radiative transfer mainly consists of two steps, inward and outward recurrence (with boundary conditions applied at the top and bottom of the atmosphere). Here formalism is given only for inward recurrence since the same procedure applies to the outward recurrence with a flip of the recurrence direction.

Starting from a reference point $\boldsymbol{R}_n$ on the outer boundary on the nth layer, the radiation field at the grid point $\boldsymbol{R}_{n+1}$ on the inner boundary in direction $\boldsymbol{\Omega}_{\mathrm{G}}$ (converted from $\boldsymbol{\Omega}_{\mathrm{L}}$ via $\boldsymbol{\Omega}_{\mathrm{G}}=\mathbf{B}(\boldsymbol{R}_{n+1})\cdot\boldsymbol{\Omega}_{\mathrm{L}}$) can be expressed as

$$\mathbf{I}^{-}(\boldsymbol{R}_{n+1},\boldsymbol{\Omega}_{\mathrm{G}})=\mathbf{I}^{-}(\boldsymbol{R}_{n},\boldsymbol{\Omega}_{\mathrm{G}})T(n,\boldsymbol{\Omega}_{\mathrm{G}})+\mathbf{I}^{-}_{\mathrm{ss}}(\boldsymbol{R}_{n+1},\boldsymbol{R}_{n};\boldsymbol{\Omega}_{\mathrm{G}})+\mathbf{I}^{-}_{\mathrm{ms}}(\boldsymbol{R}_{n+1},\boldsymbol{R}_{n};\boldsymbol{\Omega}_{\mathrm{G}}) \tag{19}$$

where $\mathbf{I}^{-}(\boldsymbol{R}_n,\boldsymbol{\Omega}_{\mathrm{G}})$ is the downward radiation field at $\boldsymbol{R}_n$ in direction $\boldsymbol{\Omega}_{\mathrm{G}}$ (with $\boldsymbol{R}_n=\boldsymbol{R}_{n+1}-\boldsymbol{\Omega}_{\mathrm{G}}\|\boldsymbol{R}_{n+1}-\boldsymbol{R}_n\|$) and, defining $\boldsymbol{R}(\ell)=\boldsymbol{R}_n+\boldsymbol{\Omega}_{\mathrm{G}}\ell$ with ℓ being the distance to the reference point $\boldsymbol{R}_n$ in direction $\boldsymbol{\Omega}_{\mathrm{G}}$, $T(n,\boldsymbol{\Omega}_{\mathrm{G}})$ is the probability of direct transmission from $\boldsymbol{R}_n$ to $\boldsymbol{R}_{n+1}$ evaluated as

$$T(n,\boldsymbol{\Omega}_{\mathrm{G}})=\exp\left[-\int_0^{\|\boldsymbol{R}_{n+1}-\boldsymbol{R}_n\|}\sigma(\boldsymbol{R}(\ell))\mathrm{d}\ell\right]. \tag{20}$$

In Eq. (19), the single and multiple scattering contributions are integrals over relevant source functions:

$$\mathbf{I}^{-}_{\mathrm{ss}}(\boldsymbol{R}_{n+1},\boldsymbol{R}_{n};\boldsymbol{\Omega}_{\mathrm{G}})=\int_0^{\|\boldsymbol{R}_{n+1}-\boldsymbol{R}_n\|}\mathbf{J}_{\mathrm{ss}}(\boldsymbol{R}(\ell),\boldsymbol{\Omega}_{\mathrm{G}})\times\exp\left[-\int_{\|\boldsymbol{R}(\ell)-\boldsymbol{R}_n\|}^{\|\boldsymbol{R}_{n+1}-\boldsymbol{R}_n\|}\sigma(\boldsymbol{R}(\ell'))\mathrm{d}\ell'\right]\mathrm{d}\ell, \tag{21}$$

$$\mathbf{I}^{-}_{\mathrm{ms}}(\boldsymbol{R}_{n+1},\boldsymbol{R}_{n};\boldsymbol{\Omega}_{\mathrm{G}})=\int_0^{\|\boldsymbol{R}_{n+1}-\boldsymbol{R}_n\|}\mathbf{J}_{\mathrm{ms}}(\boldsymbol{R}(\ell),\boldsymbol{\Omega}_{\mathrm{G}})\times\exp\left[-\int_{\|\boldsymbol{R}(\ell)-\boldsymbol{R}_n\|}^{\|\boldsymbol{R}_{n+1}-\boldsymbol{R}_n\|}\sigma(\boldsymbol{R}(\ell'))\mathrm{d}\ell'\right]\mathrm{d}\ell. \tag{22}$$

In Eq. (21), the single scattering source functions, $\mathbf{J}_{\mathrm{ss}}$, is expressed as

$$\mathbf{J}_{\mathrm{ss}}(\boldsymbol{R},\boldsymbol{\Omega}_{\mathrm{G}})=\begin{cases}0, & \text{for } \boldsymbol{R} \text{ in shadowed region,}\\ \frac{1}{4}T(\boldsymbol{R},\boldsymbol{\Omega}_{\mathrm{G},0})\sigma(\boldsymbol{R})\omega_0(\boldsymbol{R})\mathbf{M}(\boldsymbol{\Omega}_{\mathrm{G}},\boldsymbol{\Omega}_{\mathrm{G},0};\boldsymbol{R})\boldsymbol{F}, & \text{for } \boldsymbol{R} \text{ in lit region,}\end{cases} \tag{23}$$

where $T(\boldsymbol{R},\boldsymbol{\Omega}_{\mathrm{G},0})=\exp\left[-\int_0^{\|\boldsymbol{R}_{\mathrm{T}}-\boldsymbol{R}\|}\sigma(\boldsymbol{R}'(\ell))\mathrm{d}\ell\right]$ with $\boldsymbol{R}'(\ell)=\boldsymbol{R}_{\mathrm{T}}+\boldsymbol{\Omega}_{\mathrm{G},0}\ell$. And the multiple scattering source function in Eq. (22), $\mathbf{J}_{\mathrm{ms}}$, is expressed as

$$\mathbf{J}_{\mathrm{ms}}(\boldsymbol{R},\boldsymbol{\Omega}_{\mathrm{G}})=\frac{1}{4\pi}\int_{4\pi}\sigma(\boldsymbol{R})\omega_0(\boldsymbol{R})\mathbf{M}(\boldsymbol{\Omega}_{\mathrm{G}},\mathbf{B}\cdot\boldsymbol{\Omega}'_{\mathrm{L}};\boldsymbol{R})\mathbf{I}(\boldsymbol{R},\mathbf{B}\cdot\boldsymbol{\Omega}'_{\mathrm{L}})\mathrm{d}\boldsymbol{\Omega}'_{\mathrm{L}}, \tag{24}$$

where $\mathbf{M}(\boldsymbol{\Omega}_j,\boldsymbol{\Omega}_i;\boldsymbol{R})$ is the phase matrix describing light scattering from direction $\boldsymbol{\Omega}_i$ to $\boldsymbol{\Omega}_j$ at $\boldsymbol{R}$. Since the light direction is discretized into Gauss quadrature points in local coordinate system, the integral is performed over $\boldsymbol{\Omega}'_{\mathrm{L}}$ in the above equation.

With an explicit expression of the single-scattering source term, the line integral Eq. (21) can be computed through the Gaussian quadrature along the path. The multiple scattering, namely line integral Eq. (22), is evaluated by use of Newton–Cotes formulae in closed form [22] with the knowledge of source terms $\mathbf{J}_{\mathrm{ms}}$ at the two endpoints ($\boldsymbol{R}_n$, $\boldsymbol{\Omega}_{\mathrm{G}}$) and ($\boldsymbol{R}_{n+1}$, $\boldsymbol{\Omega}_{\mathrm{G}}$), namely,

$$\mathbf{I}^{-}_{\mathrm{ms}}(\boldsymbol{R}_{n+1},\boldsymbol{R}_{n};\boldsymbol{\Omega}_{\mathrm{G}})\approx a_1(\Delta\tau_{n,1})\mathbf{J}_{\mathrm{ms}}(\boldsymbol{R}_n,\boldsymbol{\Omega}_{\mathrm{G}})+a_2(\Delta\tau_{n,2})\times\mathbf{J}_{\mathrm{ms}}(\boldsymbol{R}_{n+1},\boldsymbol{\Omega}_{\mathrm{G}}), \tag{25}$$

where $\Delta\tau_{n,1}=\sigma(\boldsymbol{R}_n)\|\boldsymbol{R}_{n+1}-\boldsymbol{R}_n\|$, $\Delta\tau_{n,2}=\sigma(\boldsymbol{R}_{n+1})\|\boldsymbol{R}_{n+1}-\boldsymbol{R}_n\|$, and as derived in [15],

$$a_1(x)=\frac{1}{x^2}(x-1+e^{-x}) \tag{26}$$

and

$$a_2(x)=\frac{1}{x^2}\left[1-(1+x)e^{-x}\right]. \tag{27}$$

The above formalism (Eqs. (19)–(27)) actually pertains to an inhomogeneous spherical atmosphere. When spherical-shell geometry is assumed, the average value of the extinction coefficient $\overline{\sigma}$ is used for $R_n\le R\le R_{n+1}$ and a_1 and a_2 have the same arguments $\Delta\tau_n=\overline{\sigma}\|\boldsymbol{R}_{n+1}-\boldsymbol{R}_n\|$ [15]. Moreover, the phase matrix and SSA only depend on layer number. Eq. (25) constitutes a recurrence relation: at the current iteration the contribution of multiple scattering in a layer of thickness ΔR_n to the radiance at a point $\boldsymbol{R}_{n+1}$ on the lower boundary of the nth layer can be updated from radiance at both outer and inner boundaries of the same layer derived from the previous iteration. In an inward/outward recurrence direction, the emergent radiance at the bottom/top of atmosphere is readily obtained. The iteration is repeated until convergence is achieved. At each iterative step, the boundary conditions have to be satisfied, namely for a point $\boldsymbol{R}_{\mathrm{T}}$ at the top of the atmosphere

$$I^{-}(R_{\mathrm{T}},\boldsymbol{\Omega}_{\mathrm{G}})=Q^{-}(R_{\mathrm{T}},\boldsymbol{\Omega}_{\mathrm{G}})=U^{-}(R_{\mathrm{T}},\boldsymbol{\Omega}_{\mathrm{G}})=V^{-}(R_{\mathrm{T}},\boldsymbol{\Omega}_{\mathrm{G}})=0 \tag{28}$$

and for a point with position vector $\boldsymbol{R}_{\mathrm{P}}$ at the (depolarizing) planetary surface,

$$I^{+}(\boldsymbol{R}_{\mathrm{P}},\boldsymbol{\Omega}_{\mathrm{G}})=\int_{2\pi}r_{\mathrm{surf}}(\boldsymbol{\Omega}_{\mathrm{G}},\mathbf{B}\cdot\boldsymbol{\Omega}'_{\mathrm{L}})I^{-}(\boldsymbol{R}_{\mathrm{P}},\mathbf{B}\cdot\boldsymbol{\Omega}'_{\mathrm{L}})\mathrm{d}\boldsymbol{\Omega}'_{\mathrm{L}} \tag{29}$$

where r_{surf} is the surface reflection function and $Q^{+}(\boldsymbol{R}_{\mathrm{P}},\boldsymbol{\Omega}_{\mathrm{G}})=U^{+}(\boldsymbol{R}_{\mathrm{P}},\boldsymbol{\Omega}_{\mathrm{G}})=V^{+}(\boldsymbol{R}_{\mathrm{P}},\boldsymbol{\Omega}_{\mathrm{G}})=0$. The symbols "+" and "−" correspond to the outward and inward radiance, respectively. For a polarizing surface, the surface reflection function r_{surf} needs to be replaced by the phase matrix for surface reflection

$$\mathbf{M}_{\mathrm{surf}}(\boldsymbol{\Omega}_{\mathrm{G}},\mathbf{B}\cdot\boldsymbol{\Omega}')=\mathbf{L}(\pi-i_2)\boldsymbol{r}_{\mathrm{surf}}(\boldsymbol{\Omega}_{\mathrm{G}},\mathbf{B}\cdot\boldsymbol{\Omega}')\mathbf{L}(-i_1) \tag{30}$$

where $\boldsymbol{r}_{\mathrm{surf}}$ is the surface reflection matrix, i_1 and i_2 are the two angles rotating the Stokes vector into and out of the reflection plane, respectively [23], and for $n=1$ or 2 the rotation matrix $\mathbf{L}(\pi-i_n)=\mathbf{L}(-i_n)=[1,\ 0,\ 0,\ 0;\ 0,\ \cos(2i_n),\ -\sin(2i_n),\ 0;\ 0,\ \sin(2i_n),\ \cos(2i_n),\ 0;\ 0,\ 0,\ 0,\ 1]$ [23]. This way, the Stokes vector of the reflected light is evaluated by

$$\boldsymbol{I}^{+}(\boldsymbol{R}_{\mathrm{P}},\boldsymbol{\Omega}_{\mathrm{G}})=\int_{2\pi}\mathbf{M}_{\mathrm{surf}}(\boldsymbol{\Omega}_{\mathrm{G}},\mathbf{B}\cdot\boldsymbol{\Omega}'_{\mathrm{L}})\boldsymbol{I}^{-}(\boldsymbol{R}_{\mathrm{P}},\mathbf{B}\cdot\boldsymbol{\Omega}'_{\mathrm{L}})\mathrm{d}\boldsymbol{\Omega}'_{\mathrm{L}} \tag{31}$$

Generally the point characterized by the position vector $\boldsymbol{R}_n$ in Eq. (25) is not contained by the grid points at the outer boundary of the nth layer. $\boldsymbol{\Omega}_G$ is not contained either in the set of discretized angular directions in local coordinate system associated to $\boldsymbol{R}_n$. Therefore, the source function $\mathbf{J}_{ms}(\boldsymbol{R}_n, \boldsymbol{\Omega}_G)$ used in Eq. (25) must be evaluated by converting Ω_G to Ω and then interpolating the source function in discretized local angular directions at the grid points on the interface $R=R_n$. Specifically, for our spherical-shell atmosphere, linear interpolation in three dimensions over (Θ, θ, ϕ) is used to get $\mathbf{J}_{ms}(\boldsymbol{R}_n, \Omega_G)$ for all Stokes components. The same interpolation is used to get $\mathbf{I}^-(\boldsymbol{R}_n, \boldsymbol{\Omega}_G)$ in Eq. (19). The inward recurrence is speeded up by using the updated inward radiation field at $\boldsymbol{R}=\boldsymbol{R}_{n+1}$ to get the inward radiance from the next layer at $\boldsymbol{I}^-(\boldsymbol{R}_{n+2}, \boldsymbol{\Omega}_G)$. Using the pseudo-spherical solution formulated in Section 2.2 as the initial guess and repeating the inward and outward recurrence, the whole radiation field throughout the atmosphere converges after a few iterations.

4. Computation

4.1. Setup

In this section, we model polarized radiative transfer in Titan's atmosphere. Titan's radius at its solid surface is 2576 km and the visible haze in 2008 extended to 500 km above it. The whole atmosphere is divided into 3 major layers as a function of altitude h, namely, $0<h\le 30$ km, $30<h\le 80$ km and $80<h\le 500$ km, due to the different aerosol properties in these layers [24]. On such a basis, each major layer is further divided into sub-layers of optical depth less than 0.0075.

The Descent Imager/Spectral Radiometer (DISR) on the Huygens probe provides the opportunity to measure the aerosol and surface properties inside Titan's atmosphere. Although the measurement was confined to the landing trajectory, the Titan atmosphere is assumed to be homogeneous in each sub-layer so that our 2D spherical-shell model applies. Under this assumption, our model takes the wavelength-dependent optical depth ($\Delta\tau_n$) and SSA ($\omega_{0,n}$) inferred from DISR's measurement for 3 major layers [24]:

$$\Delta\tau_1(\lambda)=1.012\times 10^7\lambda^{-2.339},\quad \delta(\Delta\tau_1)=10\%,$$
$$\omega_0(1)=0.9701\pm 0.02,\ \text{for } h>80\ \text{km}, \tag{32}$$

$$\Delta\tau_2(\lambda)=2.029\times 10^4\lambda^{-1.409},\quad \delta(\Delta\tau_2)=15\%,$$
$$\omega_0(2)=0.9951\pm 0.01,\ \text{for } 30<h\le 80\ \text{km}, \tag{33}$$

$$\Delta\tau_3(\lambda)=6.270\times 10^2\lambda^{-0.9706},\quad \delta(\Delta\tau_3)=15\%,$$
$$\omega_0(3)=0.9333\pm 0.02,\ \text{for } h\le 30\ \text{km}, \tag{34}$$

where λ is the wavelength in nm ($350<\lambda<1600$ nm), δ denotes the measurement uncertainty and the SSA values are specifically for $\lambda=934$ nm. In addition, the phase function of Titan aerosols was tabulated in [24]. Although Titan's atmosphere consists of both aerosols and gases, the aerosol optical depth dominates by a large factor and we neglect scattering by gases at 934.8 nm wavelength.

As described in the previous section, the model can take any surface reflection function that conserves energy at every incidence angle. However, to use the surface reflectance (r_{surf}) obtained from DISR measurement, we adopt Hapke's model [25] with parameters derived from DISR measurements [26]:

$$r_{surf}=\frac{\omega_0}{4\pi}\frac{\mu'}{\mu'+\mu}\left[P_{HG}(g,\pi-\alpha_P)B_{SH}(\alpha_P)+M(\mu',\mu)\right]B_{CB}(\alpha_P) \tag{35}$$

where ω_0 is the SSA, μ' and μ are the cosines of incidence and viewing angles, respectively, in the local coordinate system of a grid point on the surface, α_P is the phase angle, $B_{SH}(\alpha_P)$ accounts for the shadow hiding opposition effect via peak width h_S and amplitude B_{S0}:

$$B_{SH}(\alpha_P)=1+B_{S0}\left[1+\frac{1}{h_S}\tan\left(\frac{\alpha_P}{2}\right)\right]^{-1}, \tag{36}$$

$B_{CB}(\alpha_P)$ accommodates the coherent backscatter opposition effect via h_C and B_{C0}:

$$B_{CB}(\alpha_P)=1+\frac{1}{2}B_{C0}\left(1+\left\{1-\exp\left[-\frac{1}{h_C}\tan\left(\frac{\alpha_P}{2}\right)\right]\right\}\times\left[\frac{1}{h_C}\tan\left(\frac{\alpha_P}{2}\right)\right]^{-1}\right)\left[1+\frac{1}{h_C}\tan\left(\frac{\alpha_P}{2}\right)\right]^{-2}, \tag{37}$$

M is the multiple scattering term:

$$M(\mu',\mu)=P(\mu')[H(\mu)-1]+P(\mu)[H(\mu')-1]+\Lambda[H(\mu)-1][H(\mu')-1] \tag{38}$$

where $H(x)$ is Chandrasekar's H function [27] and

$$P(x)=1+\sum_{n=1}^{\infty}A_n b_n P_n(x) \tag{39}$$

$$\Lambda=1+\sum_{n=1}^{\infty}A_n^2 b_n \tag{40}$$

$$A_n=\begin{cases}\frac{(-1)^{(n+1)/2}}{n}\frac{1\times 3\times 5\times\ldots\times n}{2\times 4\times 6\times\ldots\times(n+1)}, & n=\text{odd}\\ 0, & n=\text{even}\end{cases} \tag{41}$$

where b_n are the Legendre expansion coefficients of the phase function,

$$P_{HG}(g,\alpha)=1+\sum_{n=1}^{\infty}b_n(g)P_n(\cos\alpha), \tag{42}$$

and $P_{HG}(g, \alpha)$ is the Henyey–Greenstein (HG) function [28],

$$P_{HG}(g,\alpha)=\frac{1-g^2}{[1+g^2-2g\cos\alpha]^{3/2}}, \tag{43}$$

where α is the scattering angle ($\alpha=\pi-\alpha_P$). Hence, $b_n(g)=(2n+1)g^n$. To conform to the model assumption of a homogeneous surface and utilize the DISR measurement results, the photometric properties of the surface for $\lambda=930$ nm which was measured near the landing site of Huygens probe were used for $\lambda=934.8$ nm and the whole surface. DISR data fitting gives $\omega_0=0.607\pm 0.004$, $h_S=0.039\pm 0.045$, $B_{S0}=1.00$, and $g=0.028\pm 0.070$, and additionally $h_C=0.01$ and $B_{C0}=0.41$ [26]. Noticing that Hapke's model might not conserve energy under some

situations [29], energy conservation was checked and found not to be violated at these fitting parameters.

4.2. Model verification: comparison of numerical models

To verify our new algorithm, we compared results for a Titan atmosphere-like case against a backward Monte Carlo code where each scattering event is modeled from the analytic phase function (The backward Monte Carlo code was designed by us according to [30,31] for polarized radiative transfer in a spherical atmosphere). Titan's atmosphere is a more severe test case than the terrestrial atmosphere because of the large extension of the haze (500 km above the surface) relative to the radius of the solid surface (2576 km). Instead of interpolating the tabulated values of the phase function of Titan's aerosols in [24], for verification purposes, we used a double Henyey–Greenstein function (DHG) parameterized by two

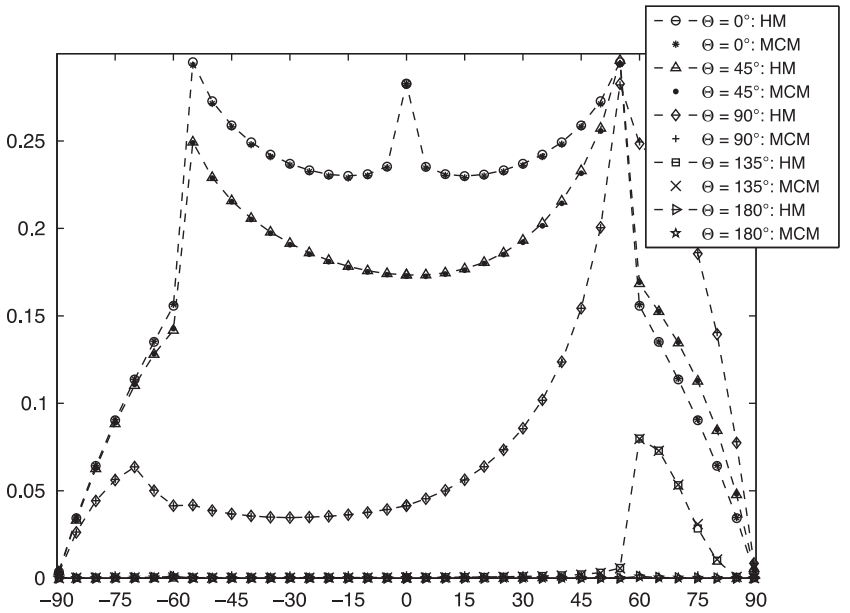

Fig. 2. Comparison of intensity (I) computed by hybrid method (HM) and backward Monte Carlo method (MCM) in the principal plane, namely with $\phi=0^\circ$ (with negative viewing angles along x-axis) as well as 180° (with positive viewing angles).

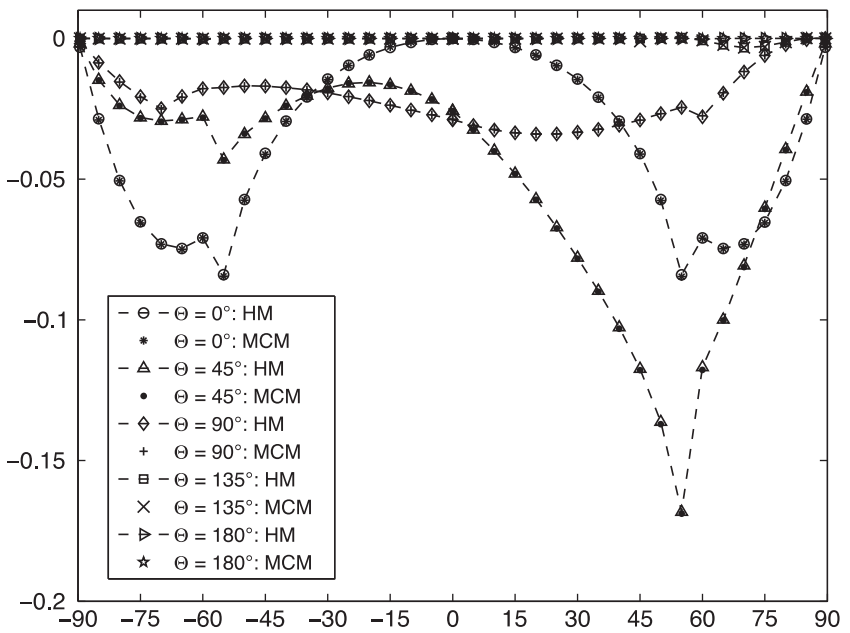

Fig. 3. Same as Fig. 2 but for the comparison of Stokes parameter Q.

asymmetry factors g_a, g_b, and a fraction factor f_a, namely,

$$P_{11}(\alpha) = f_a P_{\mathrm{HG}}(g_a,\alpha) + (1-f_a) P_{\mathrm{HG}}(g_b,\alpha). \quad (44)$$

Using the DHG, the phase function and the sampling of the new direction in the Monte Carlo method can be evaluated analytically and the sampling accuracy of the backward Monte Carlo method is thus guaranteed. To speed up the Monte Carlo computation and test whether the surface reflection is properly built into the model, we let the surface reflection have more contribution by using the smallest aerosol optical depth computed from Eqs. (32)–(34) across the wavelength range, which is 1.43 for $\lambda = 1600$ nm, and then dividing it by a scaled factor 2.9 so that total aerosol optical depth is further reduced to 0.5. The aerosols contained by Titan's haze have a highly-peaked phase function while most numerical methods, including Markov chain and Picard iteration have difficulty in efficient RT computation in their present form. Therefore δ-truncation strategies, originally proposed by Potter [32] and later designed into different forms (e.g. δ-fit [33], δ-M without [34,35] or

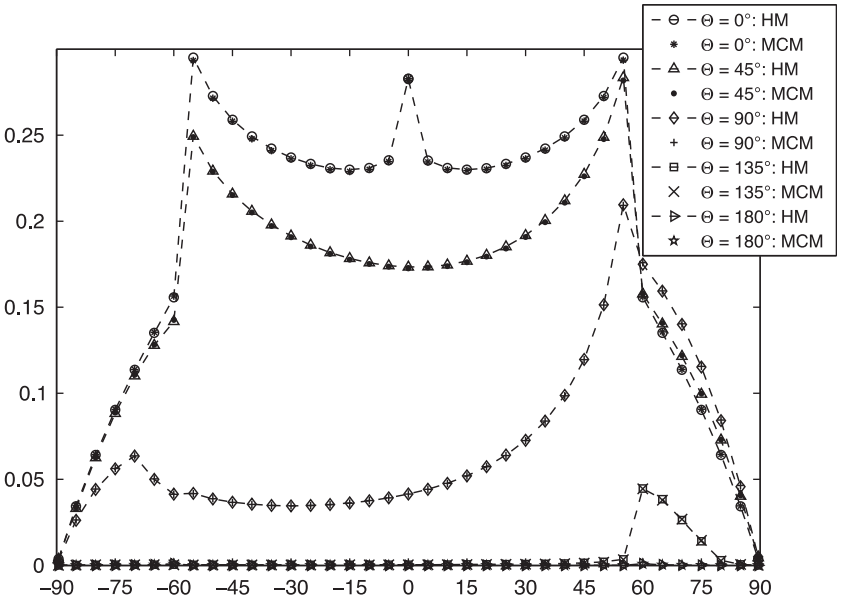

Fig. 4. Same as Fig. 2 but for the comparison of I in an off-principal plane, namely $\phi = 45^\circ$ (with negative viewing angles along x-axis) as well as 225° (with positive viewing angles).

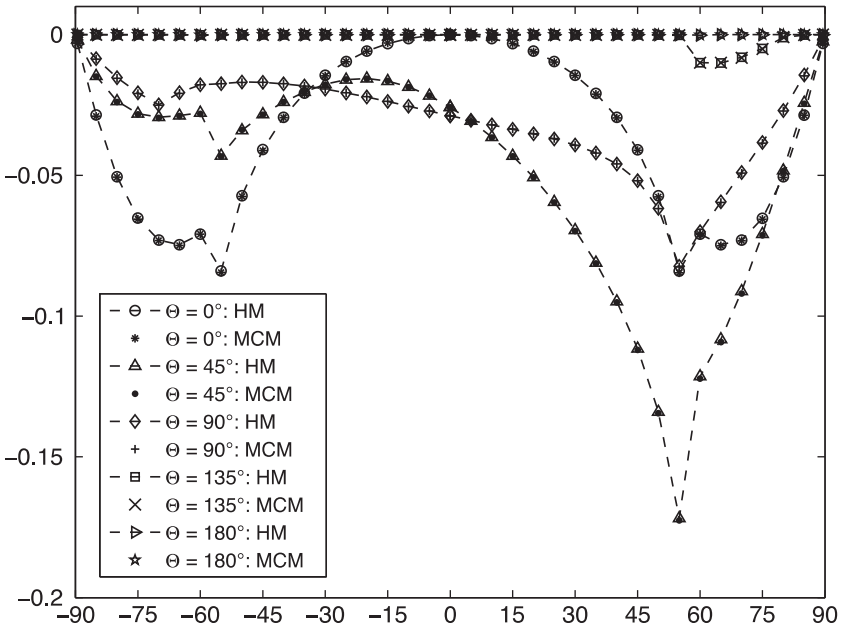

Fig. 5. Same as Fig. 4 but for the comparison of Stokes parameter Q.

with [36] intensity fluctuation correction, etc.) are widely applied by cutting off the strong forward peak and compensating the truncation by adjusting the SSA and the aerosol optical depth. To avoid the small errors introduced by δ-truncation, less forward-peaked HG functions were set for 3 aerosol layers in our testing cases, namely, $g_a(1)=0.40$, $g_b(1)=-0.10$, $g_a(2)=0.30$, $g_b(2)=-0.05$, $g_a(3)=0.20$, $g_b(3)=-0.025$, and $f_a(1)=f_a(2)=f_a(3)=0.5$. This way, δ-truncation is unnecessary and both methods give "natural" results without artificial adjustment of input parameters. Other scattering matrix entries are derived by assuming the ratio P_{ij}/P_{11} of aerosols to be similar to that of Rayleigh scattering [37,38]:

$$P_{22}(\alpha)/P_{11}(\alpha)=1 \tag{45}$$

$$P_{33}(\alpha)/P_{22}(\alpha)=2\cos\alpha/(1+\cos^2\alpha) \tag{46}$$

$$P_{12}(\alpha)/P_{11}(\alpha)=-p\sin^2\alpha/(1+\cos^2\alpha) \tag{47}$$

$$P_{34}(\alpha)/P_{11}(\alpha)=0 \tag{48}$$

where p is a scaling factor for polarization. The phase matrix is then obtained by multiplying the scattering matrix by two rotation matrices, namely [23],

$$\mathbf{M}(\mathbf{\Omega},\mathbf{\Omega}';n)=\mathbf{L}(\pi-i_2)\mathbf{P}(\text{acos}(\mathbf{\Omega}\cdot\mathbf{\Omega}');n)\mathbf{L}(-i_1). \tag{49}$$

Moreover, the angular space for the multiple scattering source function integral is discretized into 16 uniformly-spaced viewing angles in the half planes $0^\circ\le\theta\le90^\circ$ and $90^\circ\le\theta\le180^\circ$, and 27 azimuthal angles in the range $0<\phi\le360^\circ$. In addition, the domain $0\le\Theta\le180^\circ$ is divided into 181 radial lines. To generate a high polarization of aerosols, p is set to be unity as for Rayleigh scattering. Together with the setting $P_{44}(\alpha;\ n)/P_{33}(\alpha;\ n)=1$, the basic relationship of scattering matrix elements at the forward and backward scattering angles and the Cloude criterion [29] are fulfilled so that the constructed scattering matrix is physically sensible.

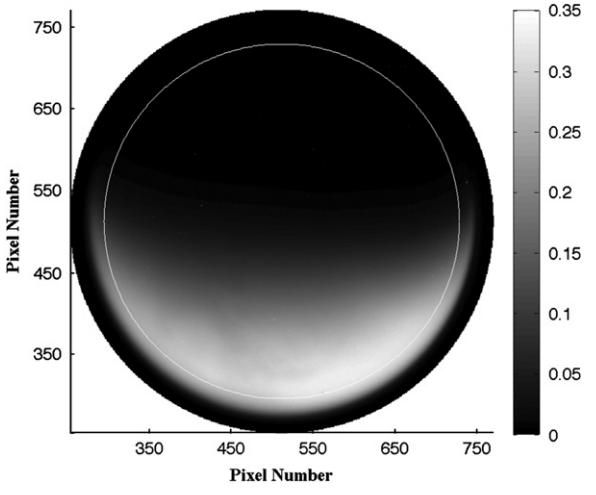

Fig. 6. I/F measured by ISS measured by ISS. The edge of Titan's solid surface is denoted by the white circle. In this and subsequent images solar illumination is from the bottom of the image.

Assuming solar flux $\pi F=\pi$ and setting the SSA $\omega_0(1)=0.92$, $\omega_0(2)=0.94$ and $\omega_0(3)=0.96$, Figs. 2 and 3 give respectively the comparison of radiance intensity I and Stokes parameter Q as a function of the local viewing angle (θ) computed by the hybrid method (HM) and the backward Monte Carlo method (MCM) in the principal plane (with local azimuthal angles $\phi=0^\circ$ and 180°). Three Picard iterations were used to get the HM results. The same comparison is made in Figs. 4 and 5 for off-principal planes (with local azimuthal angles $\phi=45^\circ$ and 225°). The radial and global angular coordinates of the point where radiation fields are displayed are $R=R_T$ (top of atmosphere) and $\Theta=0^\circ$, 45°, 90°, 135°, and $\Theta=180^\circ$, respectively ($\Theta=0^\circ$ and $\Theta=180^\circ$ correspond to the directions toward and opposite the Sun, respectively). Setting the MCM history count to 10^6, the backward Monte Carlo intensity I and Stokes parameter Q computed for $\Theta=0^\circ$, 45° and 90° and $\theta<70^\circ$ have uncertainties less than $\sim$0.5% and $\sim$5%, respectively. For both I and Q, it can be

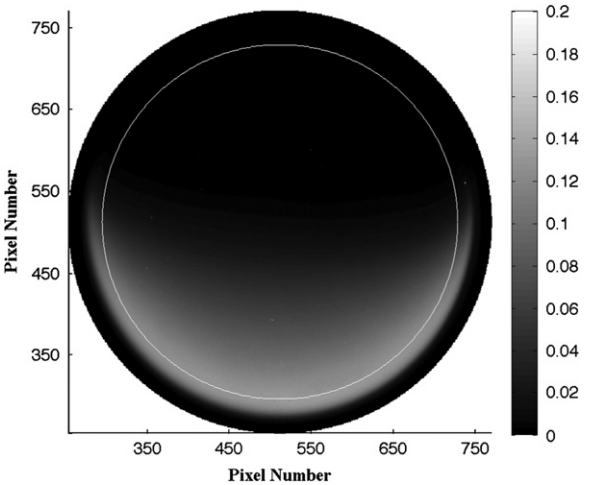

Fig. 7. $|Q|/F$ measured by ISS.

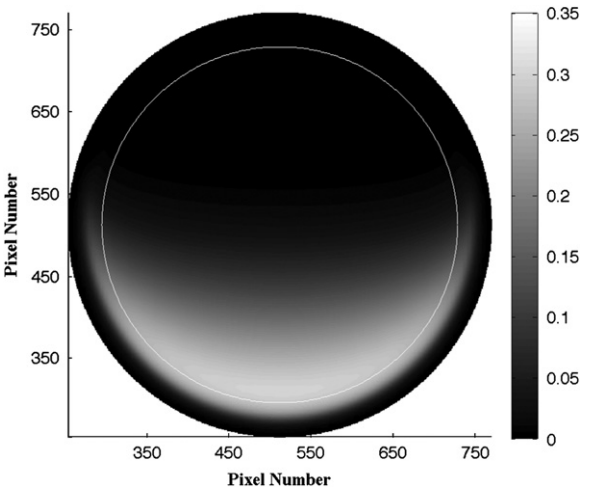

Fig. 8. I/F modeled by HM.

observed that the calculation by the HM agrees well with that of the MCM. The uncertainties for the Monte Carlo prediction, which were not plotted in Figs. 4 and 5 cover the deviation of the two methods at most angles. Moreover, it can be observed in Figs. 2–5 that, except for a directly backward scattering peak at $\theta=0^\circ$, both I and $|Q|$ have a general increase until θ approaches the transition angle $\theta_t=\mathrm{asin}(R_P/R_T)=56.7^\circ$, where the line of sight is tangential to the solid surface. Beyond θ_t, with the decrease of optical depth both I and $|Q|$ decrease to zero at $\theta=90.0^\circ$. Moreover, at the same local viewing angle $|\theta|$, the values of I and $|Q|$ at positive θ are larger than their counterparts at negative θ because the viewing ray corresponding to a negative θ angle partly traverses a region shadowed by the planet so that less illuminated atmosphere contributes to the radiation field.

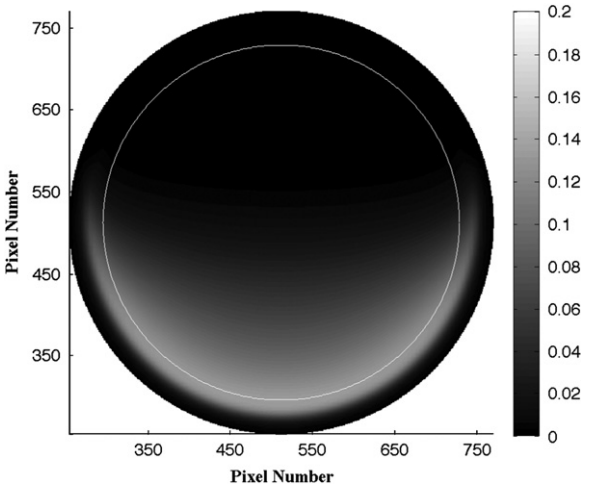

Fig. 9. $|Q|/F$ modeled by HM.

4.3. Model validation: real and simulated image comparison

To illustrate how the code described here may be used to retrieve aerosol optical properties we simulated light scattered from Titan's haze and compared the model result with the images obtained by the ISS (Imaging Science Subsystem) instrument on the Cassini spacecraft. Photopolarimetric measurements of the limb intensity can provide data to derive vertical profiles of haze properties and so we wish to accurately model the limb radiance and polarization as well as the radiance and polarization closer to the nadir.

We chose two images of Titan (IDs W1604461118 and W1604461260) from day 309 of 2008. At that time Titan's haze could be seen by the ISS cameras to extend to about 500 km altitude. Both images were taken with the CB3 filter (central wavelength near 934 nm). At this wavelength the haze optical thickness is low enough to transmit surface contrast, but greatly diminished relative to the intrinsic contrast. As illustrated in Fig. 1, the phase angle of the ISS camera was 94.7° when the measurements were made. Image W1604461118 was coupled to the IRP0 polarizing filter (passes light with the electric vector in the vertical direction in the image plane) and W1604461260 was coupled to the IRP90 filter. Both filters transmit more than 90% of the light whose electric vector oscillates in the plane parallel to the polarizing direction and less than 1% of the perpendicular electric vector is transmitted. Together these can be combined to yield intensity and Stokes parameter $|Q|$ defined with respect to the image coordinates (see [39]). The image was calibrated using the CISSCAL software [39]. As a result, Fig. 6 shows the image of I/F where I is the reflected

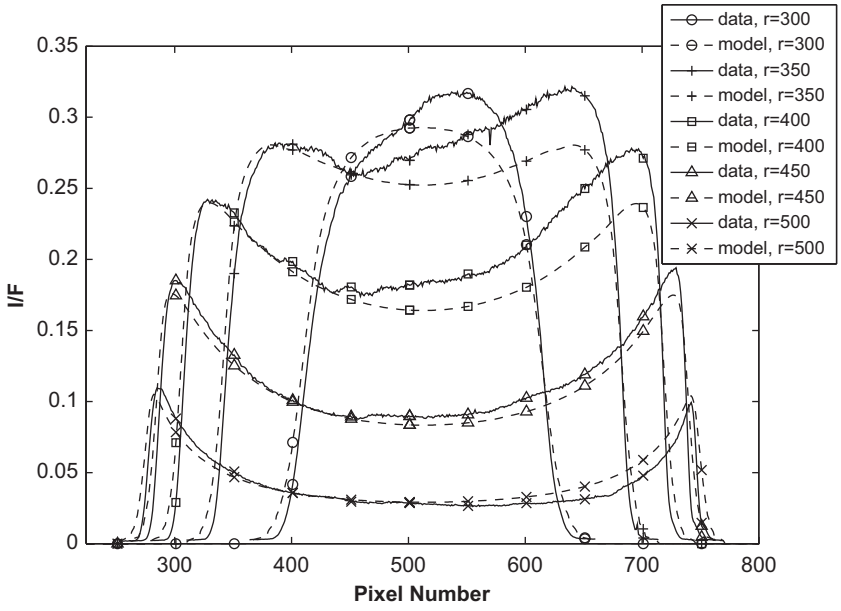

Fig. 10. Separate view of the measured and modeled I/F at the pixel rows (r) 300, 350, 400, 450, and 500.

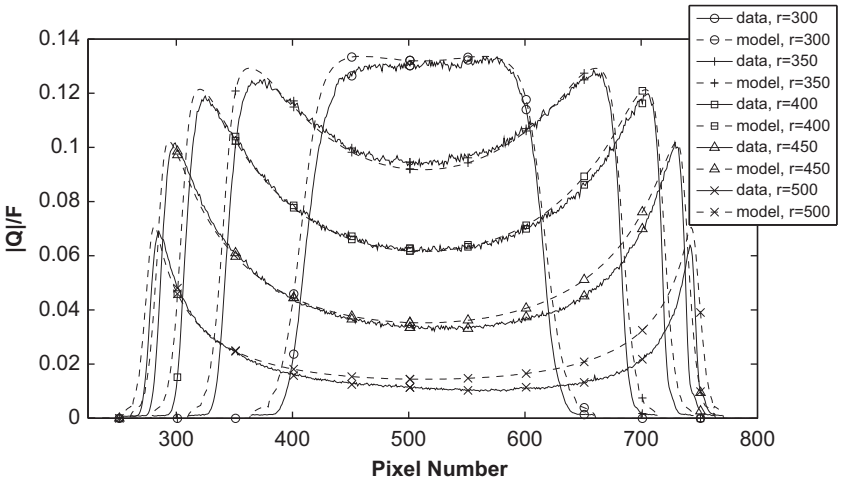

Fig. 11. Same as Fig. 10 but for $|Q|/F$ comparison.

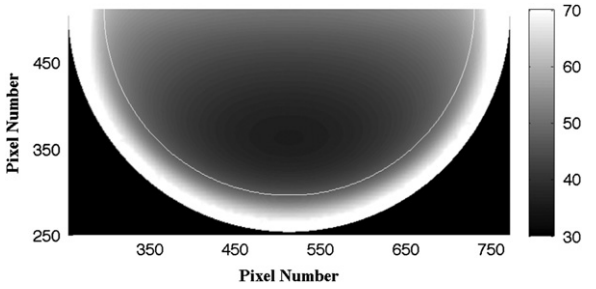

Fig. 12. Degree of linear polarization (%) in the lower half image plane modeled by HM.

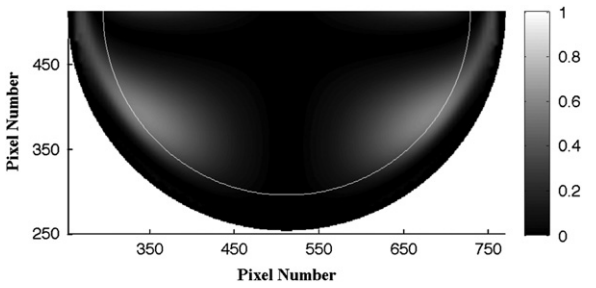

Fig. 13. $|\text{DOLP}-|Q|/I| \times 100$ in the lower half image plane modeled by HM.

intensity and πF is the solar flux and Fig. 7 shows the image of $|Q|/F$.

As described in Section 4.1, the aerosol properties and surface reflectance derived from DISR measurements [24,26] are used to simulate the images. With the setting $p=0.98$ (p is the only free parameter in our model), the phase matrix is constructed from Eqs. (45)–(48) and $P_{44}(\alpha;\ n)/P_{33}(\alpha;\ n)=1$. The scale height of the outmost layer is inferred to be 65 km according to DISR measurements (with an uncertainty of 20 km) [23]. The modeled I/F and $|Q|/F$ images are illustrated in Figs. 8 and 9. Intensity along several pixel rows from Fig. 10 indicates increasing deviation close to the limb. Near the sub-solar point at the limb however, the modeled and measured $|Q|/F$ have better agreement, as indicated by Fig. 11. Differences between modeled I/F and $|Q|/F$ can be traced to Titan's haze being not perfectly symmetric and the surface contrasts are not modeled. Moreover, the measured aerosol and surface properties along the DISR landing trajectory may not hold at locations far from the landing site and we have not attempted to fit all latitudes and altitudes by optimizing parameters. As a supplement, Fig. 12 gives the modeled image degree of polarization (DOLP) which is defined to be $(Q^2+U^2+V^2)^{1/2}/I$. Though DOLP is not measured by ISS, it can be well represented by the measured results of $|Q|/I$ since $|\text{DOLP}-|Q|/I|$ is found to be less than 1% in Fig. 13. This is due to the very small contribution of U when the polarizers are aligned parallel and perpendicular to the scattering plane.

5. Summary and outlook

We have developed a hybrid method to compute the Stokes vector field throughout a vertically extended spherical atmosphere. The method starts with a Markov chain computation of the Stokes vector field inside a pseudo-spherical atmosphere. The new forward model was tested against the backward Monte Carlo method for a synthetic atmosphere with different aerosol properties in three layers, resulting in excellent agreement for both intensity I and Stokes parameter Q. With the knowledge of Titan's aerosol and surface properties derived from DISR measurements, the images of I/F and $|Q|/F$ were modeled and compared to the real ones measured by ISS at 934.8 nm. To reduce the deviation of the modeled I/F and $|Q|/F$ and the measured ones, better knowledge of aerosol and surface properties needs to be obtained, which forms the target of our future work. Specifically, we will use the limb-viewing radiance and Q for aerosol retrievals where the contribution of surface is small. With improved knowledge of aerosol properties, the surface can be better retrieved with the aid of the spherical RT model.

Acknowledgments

This work was done at the Jet Propulsion Laboratory, California Institute of Technology under contract with the National Aeronautics and Space Administration. One of the authors (F. Xu) is grateful to Professor Larry Esposito at the University of Colorado for assistance during his pursuit of developing the Markov chain formalism for polarized reflectance computation for plane-parallel atmosphere, and Dr. Philip Dumont at the Jet Propulsion Laboratory for some helpful discussions regarding the iterative method for modeling radiative transfer in Titan's atmosphere. We thank the anonymous reviewers for their thorough evaluation and constructive comments for improving the paper.

References

[1] DeLuisi JJ, Mateer CL. On the application of the optimum statistical inversion technique to the evaluation of Umkehr observations. J Appl Meteorol 1971;10:328–34.
[2] Caudill TR, Flittner DE, Herman BM, Torres O, McPeters RD. Evaluation of the pseudo-spherical approximation for backscattered ultraviolet radiances and ozone retrieval. J Geophys Res 1997;102(D3):3881–90.
[3] Petropavlovskikh I, Loughman R, Deluisi J, Herman BA. Comparison of UV intensities calculated by spherical-atmosphere radiation transfer codes: application to the aerosol corrections. J Geophys Res 2000;105(D11):14737–46.
[4] Spurr RJD. VLIDORT: a linearized pseudo-spherical vector discrete ordinate radiative transfer model for forward model and retrieval studies in multilayer multiple scattering media. J Quant Spectrosc Radiat Transfer 2006;102:316–42.
[5] Collins DG, Blättner WG, Wells MB, Horak HG. Backward Monte Carlo calculations of the polarization characteristics of the radiation emerging from spherical-shell atmospheres. Appl Opt 1972;11: 2684–96.
[6] Vincendon M, Langevin Y. A spherical model Monte-Carlo model of aerosols: validation and first applications to Mars and Titan. ICARUS 2010;207:923–31.
[7] Tran TT, Rannou P. Comparing 3D spherical Monte-Carlo and 2-stream parallel-plane simulations of far-field backscattering image of Titan. Notes du Pole 2, Inst Pierre Simon Laplace, Paris; 2004.
[8] Bourassa AE, Degenstein DA, Llewellyn EJ. SASKTRAN: a spherical geometry radiative transfer code for efficient estimation of limb scattered sunlight. J Quant Spectrosc Radiat Transfer 2008;109: 52–73.
[9] Herman BM, Ben-David A, Thome KJ. Numerical technique for solving the radiative transfer equation for a spherical shell atmosphere. Appl Opt 1994;33:1760–70.
[10] Herman BM, Caudill TR, Flittner DE, Thome KJ, Ben-David A. Comparison of the Gauss-Seidel spherical polarized radiative transfer code with other radiative transfer codes. Appl Opt 1995;34:4563–72.
[11] Kuo KS, Weger RC, Welch RM, Cox SK. The Picard iterative approximation to the solution of the integral equation of radiative transfer. Part II: three-dimensional geometry. J Quant Spectrosc Radiat Transfer 1996;55:195–213.
[12] Stenholm LG, Storzer H, Wehrse W. An efficient method for the solution of 3D radiative transfer methods. J Quant Spectrosc Radiat Transfer 1991;45:47–56.
[13] Rozanov A, Rozanov V, Burrows JP. A numerical radiative transfer model for a spherical planetary atmosphere: combined differential-integral approach involving the Picard iterative approximation. J Quant Spectrosc Radiat Transfer 2001;69:491–512.
[14] Salinas SV, Grieger B, Markiewicz WJ, Keller HU. A spherical model for computing polarized radiation in Titan's atmosphere. Planet Space Sci 2003;51:977–89.
[15] Doicu A, Trautmann T. Picard iteration methods for a spherical atmosphere. J Quant Spectrosc Radiat Transfer 2009;110:1851–63.
[16] Esposito LW, House LL. Radiative transfer calculated by a Markov chain formalism. Astrophys J 1978;219:1058–67.
[17] Esposito LW. An 'adding' algorithm for the Markov chain formalism for radiation transfer. Astrophys J 1979;233:661–3.
[18] Chandrasekhar S. Radiative Transfer. New York: Dover; 1960.
[19] Xu F, Davis AB, West RA, Esposito LW. Markov Chain formalism for polarized light transfer in plane-parallel atmospheres, with numerical comparison to the Monte Carlo method. Opt Express 2011;19: 946–67.
[20] Xu F, Davis AB, West RA, Martonchik JV, Diner DJ. Markov chain formalism for vector radiative transfer in a plane-parallel atmosphere overlying a polarizing surface. Opt Lett 2011;36:2083–5.
[21] Caudill TR. Accuracy of the total ozone mapping spectrometer at polar latitudes. PhD dissertation. University of Arizona: Tucson; 1994.
[22] Abramowitz M, Stegun IA, editors. New York: Dover; 1972.
[23] Hovenier JW. Symmetry relations for scattering of polarized light in a slab of randomly oriented particles. J Atmos Sci 1969;26:488–99.
[24] Tomasko MG, Doose L, Engel S, Dafoe LE, West R, Lemmon M, et al. A model of the aerosols in Titan's aerosols based on measurements made inside the atmosphere. Planet Space Sci 2008;56:669–707.
[25] Hapke B. Bidirectional reflectance spectroscopy 5. Coherent backscatter opposition effect and anisotropic scattering. ICARUS 2002;157:523–34.
[26] Schröder SE, Keller HU. The unusual phase curve of. Titan's surface observed by Huygens' Descent Imager/Spectral Radiometer. Planet Space Sci 2009;57:1963–74.
[27] Chandrasekhar S. Radiative Transfer. New York: Dover; 1960.
[28] Henyey LG, Greenstein JL. Diffuse radiation in the galaxy. Astrophys J 1941;93:70–83.
[29] Mishchenko MI, Macke A. Asymmetry parameters of the phase function for isolated and densely packed spherical particles with multiple internal inclusions in the geometric optics limit. J Quant Spectrosc Radiat Transfer 1997;57:767–94.
[30] Collins DG, Blättner WG, Wells MB, Horak HG. Backward Monte Carlo calculations of the polarization characteristics of the radiation emerging from spherical-shell atmospheres. Appl Opt 1972;11:2684–96.
[31] Spada F, Krol MC, Stammes P. McSCIA: application of the Equivalence Theorem in a Monte Carlo radiative transfer model for spherical shell atmospheres. Atmos Chem Phys 2006;6:4823–42.
[32] Potter JF. The delta function approximation in radiative transfer. J Atmos Sci 1970;27:943–9.
[33] Hu YX, Wielicki B, Lin B, Gibson G, Tsay SC, Stamnes K, et al. δ-fit: a fast and accurate treatment of particle scattering phase functions with weighted singular-value decomposition least-squares fitting. J Quant Spectrosc Radiat Transfer 2000;65:681–90.
[34] Wiscombe WJ. The delta-M method: rapid yet accurate radiative flux calculations for strongly asymmetric phase functions. J Atmos Sci 1977;34:1408–22.
[35] Min Q, Duan M. A successive order of scattering model for solving vector radiative transfer in the atmosphere. J Quant Spectrosc Radiat Transfer 2004;87:243–59.
[36] Nakajima T, Tanaka M. Algorithms for radiative intensity calculations in moderately thick atmospheres using a truncation approximation. J Quant Spectrosc Radiat Transfer 1988;40:51–69.
[37] White RL. Polarization in reflection nebulae. I. Scattering properties of interstellar grains. Astrophys J 1979;229:954–61.
[38] Braak CJ, de Haan JF, van der Mee CVM, Hovenier JW, Travis LD. Parameterized scattering matrices for small particles in planetary atmospheres. J Quant Spectrosc Radiat Transfer 2001;69:585–604.
[39] West R, Knowles B, Birath E, Charnoz S, di Nino D, Hedman M, et al. In-flight calibration of the Cassini imaging science sub-system cameras. Planet Space Sci 2010;58:1475–88.